Article

Modeling and Compound Closed-Loop Control of Single-Phase Quasi-Single-Stage Isolated AC-DC Converter

Fengjiang Wu [ID]**, Guangfu Hu and Jianyong Su *** [ID]

Department of Electrical Engineering, Harbin Institute of Technology, Harbin 150001, China
* Correspondence: sujianyong@hit.edu.cn

Abstract: The single-phase isolated quasi-single-stage AC-DC converter has many virtues, such as high power density and efficiency; however, its grid current closed-loop control has not been solved. This paper aims to solve the remaining gap based on a large-signal model. In this paper, the large-signal model of this converter under triple-phase-shift modulation is built for the first time. It is verified that the built model is a zero-order linear system. Based on this built model, the effect of grid harmonics on this converter grid current is analyzed. The theoretical analysis reveals that the grid voltage low-order harmonics will cause the same order grid current harmonics and only varying the parameters of the filter is not an effective method to solve this problem. For the purpose of eliminating the effect of grid voltage harmonics on the grid current and realizing the zero-error control of the fundamental component of the grid current, a grid current closed-loop control strategy based on the proportional-resonant compound odd-mode repetitive controller is proposed. The operation principle, parameter constraint, and design rule of the proposed compound control strategy are analyzed comprehensively. The theoretical analysis and the compound control strategy put forward in this paper are tested, with detailed experimental results.

Keywords: isolated AC-DC converter; single phase; large-signal model; compound current controller

1. Introduction

With the development of renewable energy generation and energy storage technologies, isolated AC-DC converters become more and more attractive. Isolated AC-DC converters generally include two-stage AC-DC-DC structures [1–6] and single-stage ones. The two-stage structures possesses good performance, however, because of the large DC link capacitor, the power density and lifetime are difficult to increase [7–9], which is the main disadvantage of this structure.

Over the past few years, single-phase isolated quasi-single-stage (Q1S) AC-DC converters without DC link electrolytic capacitors have been put forward [10–13]. Their front-end rectifier operates at the grid frequency, for which the switching loss can be ignored [14]. Its back dual-active-bridge (DAB) converter can adopt an optimized phase shift modulation. In [15], a triple-phase-shift (TPS) modulation strategy is proposed to extend the range of the soft-switching operation. A closed-form analytical solution for the modulation scheme of full-range zero-voltage-switching (ZVS) and near-minimum circulating currents is presented in [16], which improves the efficiency and lifetime of the converter. Thanks to the efforts of researchers, this type of converter provides an effective solution to enhance the power density and efficiency and lengthen the lifetime of grid-connected power-conversion systems.

Since this type of converter needs to be generally connected to power grid, its quality of the grid current waveform ought to be ensured, otherwise the corresponding grid-connected standard cannot be reached. Based on its working principle, the voltage and current of the back-end DAB converter are processed in sinusoidal form, which illustrates that port voltage and average transfer current in a switching cycle are different from those in

the contiguous cycle. Instantaneous transformer currents in any two contiguous switching cycles should be uncoupled and independently controlled so as to achieve the goal of average transfer current without steady-state error. In [17], an improved triple-phase-shift (ITPS) modulation strategy is put forward, in order to completely eliminate circulating currents and coupling of transformer currents in the contiguous switching cycles, thus realizing the accurate control of AC side transfer currents. As a result, AC side currents of this converter are sine waves.

Under ideal conditions, namely, if the grid voltage waveform is sinusoidal without any harmonics, the grid current waveform will also be sinusoidal because the ITPS ensures a sinusoidal waveform of the AC side average current of the converter. However, an LC filter is set up between the converter and grid, which can transform converter's AC side discrete currents to be continuous sine waveforms of grid currents. The LC filter introduces an impedance link between the grid and the converter, and as a result, the grid current is determined not only by AC side currents together but also by grid voltages. Since low-order harmonics are generally included in actual grid voltages, grid currents are difficult to ensure good sine waves, even though AC side currents of this converter are perfect sine waves. For the grid-connected type converters, the general solution to eliminate the influence of grid harmonics on grid currents is to construct the closed-loop control configuration of grid currents. In [18], a ripple controller with improved voltage feed-forward scheme and quasi-proportional-resonant compensator was designed to realize good voltage ripple suppression for a Q1S AC–DC converter with an audio susceptibility model. A Q1S current-fed resonant AC-DC converter is proposed in [19]. Its closed-loop control adopts a dual-loop structure, whose inner loop is used to control the grid current and the outer loop regulates the output voltage. A PI controller is used in both inner loop and outer loop. In [20], a hybrid control strategy was proposed to realize stable output voltage and quasi-constant bus voltage, which consists of the output voltage feedback loop and the bus voltage feedback loop. However, the influence of the grid voltage harmonics on grid currents is not considered in [18–20].

In order to eliminate the influence of the grid harmonics on grid currents of the Q1S AC-DC converter and fill in research gaps, in this paper, this problem is deeply researched and a grid current closed-loop control strategy for this converter is proposed. This paper has the following innovations and contributions. (1) The large-signal model of the Q1S AC-DC converter is built for the first time. (2) The influence of the grid voltage harmonics on grid currents is derived, which builds the theoretical basis for the upcoming solutions. (3) A novel grid current closed-loop control strategy is put forward by combining proportional-resonant (PR) controllers and odd-mode repetitive controllers (OMRC). The proposed closed-loop control strategy realizes the control of grid currents without steady-state error and eliminates the influence from grid voltage harmonics.

The rest of this paper is organized as follows. Section 2 introduces the process of building the large-signal model of the Q1S AC-DC converter. In Section 3, the influence of grid harmonics on grid currents is discussed based on the built model. In Section 4, a novel compound grid current closed-loop control strategy containing a PR controller and an OMRC is proposed. Then, parameter constraints of the proposed compound controller are discussed. Section 5 shows the experimental results. Finally, the conclusion is presented in Section 6.

2. Large-Signal Model of Q1S AC-DC Converter

For the purpose of analyzing the influence of grid voltage low-order harmonics on grid currents, the large-signal model of the Q1S AC-DC converter under ITPS is built.

Figure 1 shows the topology structure of the Q1S AC-DC converter, which is comprised of the front-end synchronous rectifier and the back-end DAB converter. Its front-end synchronous rectifier converts the grid voltage to the unipolar rectified waveform. Comprised of the DC side capacitor C_1 and AC side inductor L_g, the LC filter can filter out the high-frequency current components before they flow into the grid. Thus, the capacitance of

C_1 is generally very small and not exceeding tens of micro-Farad. HB1 and HB2 represent two H-bridge converters. v_p and v_s are the high-frequency voltages of HB1 and HB2. v_{dc1} and v_{dc1} are DC side voltages, and i_{dc1} and i_{dc2} are DC side currents. i_p represents the primary current of the high-frequency transformer (HFT). The turns ratio is n.
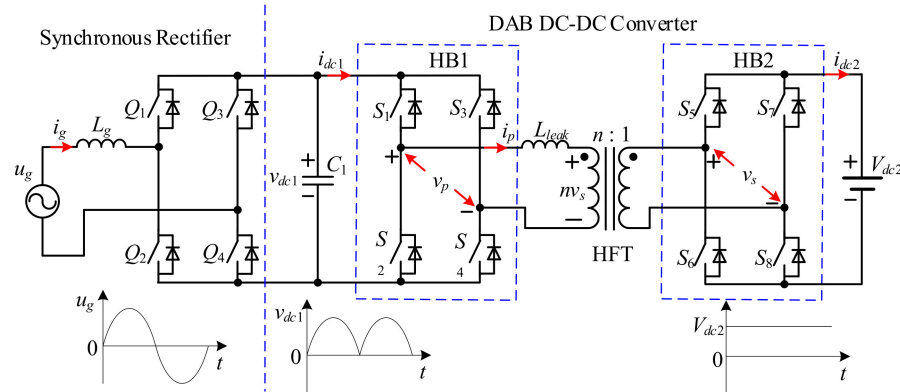

Figure 1. Schematic of Q1S AC-DC converter.

After the grid voltage is rectified, the unipolar voltage v_{dc1} can be acquired on C_1. The expression is shown as

$$v_{dc1} = V_m |\sin(\omega_1 t)| \tag{1}$$

In (1), V_m and ω_1 represent amplitude and frequency of the grid voltage.

For the purpose of keeping sinusoidal grid current i_g, the expected average DC side current of HB1 in the switching cycle $\langle i_{dc1} \rangle^*_{T_S}$ should be sinusoidal. As reported in [17], its definition is

$$\langle i_{dc1} \rangle^*_{T_S} = I_m^* |\sin(\omega_1 t)| \tag{2}$$

In (2), I_m^* is the expected AC side current amplitude of this converter. Since the grid frequency is far less than DAB converter's switching frequency, v_{dc1} can be deemed a constant. Thus, at the switching cycle scale, the principle of the DAB converter put behind and exhibited in Figure 1 identifies with the routine DAB DC-DC converter. Then this converter can realize the function of AC-DC buck-boost voltage conversion and bidirectional power flow. In [17], an ITPS modulation strategy is proposed to completely eliminate the circulating current and make transformer currents uncoupled in adjacent switching cycles, thus realizing the AC side transfer current's accurate control of the converter. Switching period scale operating waves of the ITPS put forward in [17] are shown in Figure 2. In Figure 2, the voltage conversion ratio is $k = v_{dc1}/nV_{dc2}$, $\langle i_{dc1} \rangle_{T_S\_cri1} = \frac{v_{dc1} T_S}{4 L_{leak}} \frac{k-1}{k^3}$. D_1 and D_2 represent the internal phase angles of HB1 and HB2, while D_φ represents the outer phase shift angle.

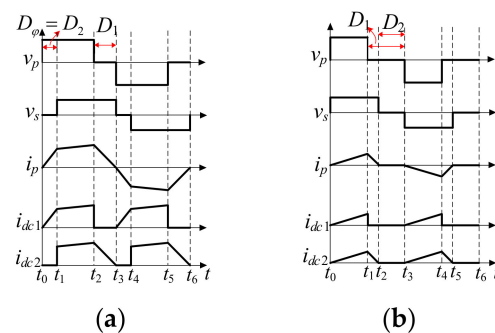**Figure 2.** Switching period scale operating waveforms of ITPS. (a) $k > 1$, $\langle i_{dc1} \rangle^*_{T_S} > \langle i_{dc1} \rangle_{T_S\_cri1}$, (b) $k > 1$, $\langle i_{dc1} \rangle^*_{T_S} \le \langle i_{dc1} \rangle_{T_S\_cri1}$.

From Figure 2, transformer currents of the contiguous switching cycles are decoupled and waveforms of the positive half switching cycle and the negative half switching period

are completely symmetrical. For the sake of the simplification, the large-signal model is derived based on the waveforms in the positive half switching period. From Figure 1, the grid side filter inductor, capacitor, and transformer leakage inductor are energy-storage components in this converter. Therefore, i_g, v_{dc1} and are selected as the state variables for the large-signal model building of this converter.

Based on Figures 1 and 2a, the state equation i_p during $t \in [t_0, t_3)$ is expressed as (3) in [17].

$$\frac{di_p}{dt} = \frac{v_p - nv_s}{L_{leak}} = \begin{cases} \frac{v_{dc1}}{L_{leak}}, & [t_0, t_1) = D_\varphi \frac{T_S}{2} \\ \frac{v_{dc1} - nV_{dc2}}{L_{leak}}, & [t_1, t_2) = (1 - D_1 - D_\varphi) \frac{T_S}{2} \\ \frac{-nV_{dc2}}{L_{leak}}, & [t_2, t_3) = D_1 \frac{T_S}{2} \end{cases} \tag{3}$$

By putting three phase shifts' relationships of the ITPS in [16] into (3), the variation rate of the average transformer current within a half switching cycle is

$$L_{leak} \frac{d\langle i_p \rangle_{T_S}}{dt} = \frac{2}{T_S} \left(\int_0^{D_\varphi \frac{T_S}{2}} \left(\frac{v_{dc1}}{L_{leak}} \right) dt + \int_0^{D_1 \frac{T_S}{2}} \left(\frac{-nV_{dc2}}{L_{leak}} \right) dt \\ + \int_0^{(1-D_1-D_\varphi) \frac{T_S}{2}} \left(\frac{v_{dc1} - nV_{dc2}}{L_{leak}} \right) dt \right) \equiv 0 \tag{4}$$

From Figures 1 and 2a, the state equation of v_{dc1} during $t \in [t_0, t_3)$ is expressed as

$$C_1 \frac{dv_{dc1}}{dt} = \begin{cases} i_g - i_p, & t \in [t_0, t_1) \\ i_g - i_p, & t \in [t_1, t_2) \\ i_g - 0, & t \in [t_2, t_3) \end{cases} \tag{5}$$

The average value of (5) within a half switching cycle is

$$C_1 \frac{dv_{dc1}}{dt} = i_g - \frac{2}{T_S} \left(\int_{t_0}^{t_1} i_p dt + \int_{t_1}^{t_2} i_p dt \right) = i_g - \langle i_{dc1} \rangle_{T_S} \tag{6}$$

The state equation of i_g in the positive half switching cycle is acquired from Figure 1:

$$L_g \frac{di_g}{dt} + i_g r_L = u_g - v_{dc1}, \quad t \in [t_0, t_3) \tag{7}$$

r_L in (7) is called the filter parasitic resistor of the filter inductor. On the basis of (4), (6), and (7), the large-signal model of the converter under the modulation in Figure 2b is

$$\frac{d}{dt} \begin{bmatrix} \langle i_p \rangle_{T_S} \\ v_{dc1} \\ i_g \end{bmatrix} = \begin{bmatrix} 0 & 0 \\ 1/C_1 & 0 \\ -r_L & 1/L_g \end{bmatrix} \begin{bmatrix} i_g \\ u_g \end{bmatrix} + \begin{bmatrix} 0 & 0 \\ -1/C_1 & 0 \\ 0 & -1/L_g \end{bmatrix} \begin{bmatrix} \langle i_{dc1} \rangle_{T_S} \\ v_{dc1} \end{bmatrix} \tag{8}$$

Similarly, the large-signal model in the negative half grid cycle is derived as

$$\frac{d}{dt} \begin{bmatrix} \langle i_p \rangle_{T_S} \\ -v_{dc1} \\ i_g \end{bmatrix} = \begin{bmatrix} 0 & 0 \\ 1/C_1 & 0 \\ -r_L & 1/L_g \end{bmatrix} \begin{bmatrix} i_g \\ u_g \end{bmatrix} - \begin{bmatrix} 0 & 0 \\ -1/C_1 & 0 \\ 0 & -1/L_g \end{bmatrix} \begin{bmatrix} \langle i_{dc1} \rangle_{T_S} \\ v_{dc1} \end{bmatrix} \tag{9}$$

In order to characterize (8) and (9) in a unified form, define the following variables.

$$v_{dc1\_u} = \begin{cases} v_{dc1} & Q_1 \& Q_4 = 1 \\ -v_{dc1} & Q_2 \& Q_3 = 1 \end{cases}$$
$$i_{av1\_u} = \begin{cases} \langle i_{dc1} \rangle_{T_S} & Q_1 \& Q_4 = 1 \\ -\langle i_{dc1} \rangle_{T_S} & Q_2 \& Q_3 = 1 \end{cases} \tag{10}$$

From (8)–(10), the large-signal model of the Q1S AC-DC converter in the whole grid cycle is

$$\frac{\mathrm{d}}{\mathrm{d}t}\begin{bmatrix}\langle i_p\rangle_{T_S}\\ v_{dc1\_u}\\ i_g\end{bmatrix} = \begin{bmatrix}0 & 0\\ 1/C_1 & 0\\ -r_L & 1/L_g\end{bmatrix}\begin{bmatrix}i_g\\ u_g\end{bmatrix} + \begin{bmatrix}0 & 0\\ -1/C_1 & 0\\ 0 & -1/L_g\end{bmatrix}\begin{bmatrix}i_{av1\_u}\\ v_{dc1\_u}\end{bmatrix} \quad (11)$$

From (11), it is obvious that the differential value of the average transformer current in a switching cycle is zero. This feature is very interesting, because under the ITPS, L_{leak} does not cause the transient process of the transformer current, and in consequence the total order number of the system decreases. It means even the step change of the three phase shift occurs, the transformer current will reach its final value immediately, and there is no transient process; therefore, the Q1S AC-DC converter under the ITPS is a linear system in essence.

From (11), the transfer functions from u_g to i_g and from i_{av1_u} to i_g can be expressed as

$$\begin{cases} G_{u_g2i_g}(s) = \dfrac{i_g(s)}{u_g(s)} = \dfrac{sC_1}{L_gC_1s^2+r_LC_1s+1}\\[2mm] G_{i_{av}2i_g}(s) = \dfrac{i_g(s)}{i_{av1\_u}(s)} = \dfrac{1}{L_gC_1s^2+r_LC_1s+1}\end{cases} \quad (12)$$

According to (12), Figure 3 shows the bode diagrams of the built model, the simulation amplitude and phase data of the built model through the frequency-response method. From Figure 3, the theoretical bode diagrams of the built model basically coincides with the simulation data, which proves the validity of the built model.
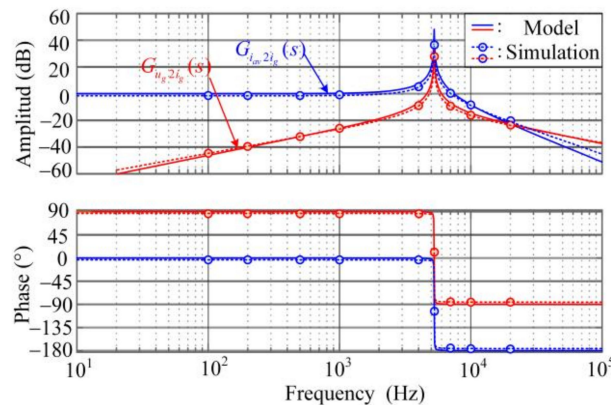

Figure 3. Bode diagrams and simulation data of various transfer functions.

3. Influence of Grid Harmonics on Grid Currents

From Figure 1, the actual grid currents are decided not only by grid voltages but also by AC side average currents of the converter. For this part, taking the low-order grid voltage harmonics into consideration, the influence of these harmonics on grid currents is researched based on the built model.

Based on the principle of ITPS in [17], AC side currents of the converter are still sine shaped even if there are low-order harmonics in grid. From its large-signal model, the converter under the ITPS can be equivalent to a controlled current source i_{av1_u}. Then when there are low-order harmonics in grid, the fundamental and harmonics equivalent circuits of this Q1S AC-DC converter are shown as Figure 4a,b, respectively.

From the fundamental equivalent circuit in Figure 4a, the relationship among various variables yields

$$\begin{cases} i_{g1} = i_{C_11} + i_{av\_u1}\\ i_{C_11} = j\omega_1C_1\cdot v_{dc1\_u}\\ v_{dc1\_u} = u_{g1} - j\omega_1L_g\cdot i_{g1} - r_Li_{g1}\end{cases} \quad (13)$$
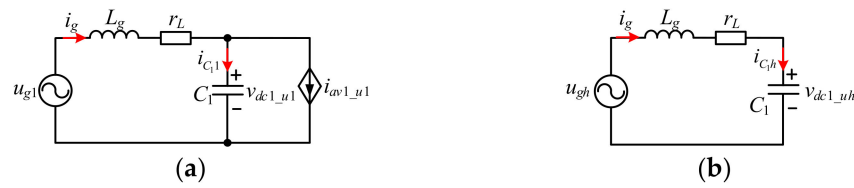
Figure 4. AC side equivalent circuits of Q1S AC-DC converter. (**a**) The fundamental equivalent circuit, (**b**) the harmonic equivalent circuit.

From (13), the grid current fundamental component is

$$i_{g1} = \frac{j\omega_1 C_1 u_{g1} + i_{av1\_u1}}{\left(1 + j\omega_1 C_1 r_L - \omega_1^2 L_g C_1\right)} \tag{14}$$

From the harmonics equivalent circuit in Figure 4b, the grid current harmonics yield

$$i_{gh} = \frac{u_{gh}}{j\omega_h L_g + 1/(j\omega_h C_1) + r_L i_{g1}} = \frac{j\omega_h C_1 u_{gh}}{\left(1 + j\omega_h C_1 r_L - \omega_h^2 L_g C_1\right)} \tag{15}$$

From (14) and (15), the expression of the total grid current yields

$$\begin{aligned} i_g &= i_{g1} + i_{gh} \\ &= \frac{j\omega_1 C_1 u_{g1} + i_{av1\_u1}}{\left(1 + j\omega_1 C_1 r_L - \omega_1^2 L_g C_1\right)} + \frac{j\omega_h C_1 u_{gh}}{\left(1 + j\omega_h C_1 r_L - \omega_h^2 L_g C_1\right)} \end{aligned} \tag{16}$$

From (16), i_{g1} is mainly determined by the currents of the converter AC side, while grid voltage low-order harmonics generate grid current harmonics, whose amplitudes are related to the LC filter parameters. The orders of those harmonics are consistent.

The effect of LC filter parameters on grid current low-order harmonics is analyzed as follows. For the parameter design of the LC filter, the ranges of the LC filter parameters should be comprehensively determined by the filter cutoff frequency, filter damping, and the power factor, and the specific parameters are finally determined according to the actual system operation performance [21]. Hence, for a certain filter resonant frequency, there are a series of LC filter parameters to be selected. Figure 5 shows the simulation waveforms of grid currents with two different groups of the filter inductance and capacitance, while with the same resonant frequency of 5 kHz. The simulation parameters of the converter are shown in Table 1. The 3rd and 5th harmonics contents in the grid voltage are 10% and 5%, respectively, and the given grid current amplitude is 5A.
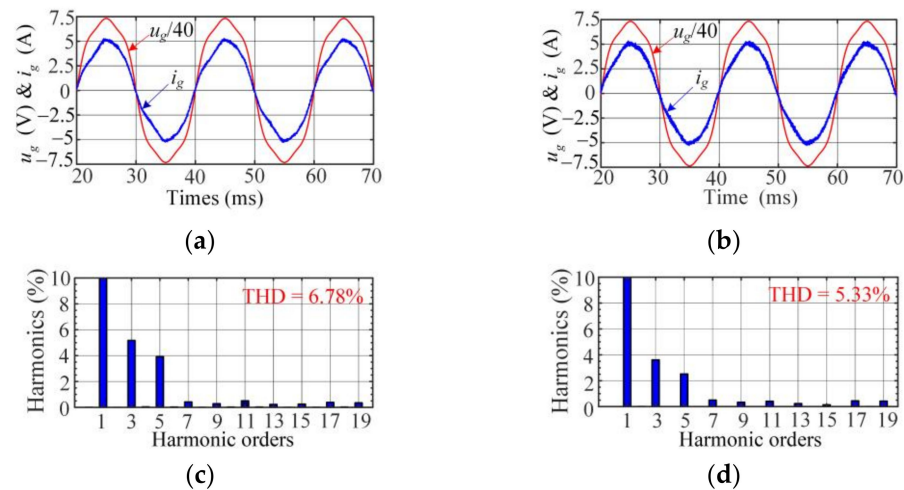

Figure 5. Simulation waveforms with different filter parameters. (**a**,**c**) 120 uH & 7.5 uF and FFT of ig, (**b**,**d**) 180 uH & 5 uF and FFT of ig.

Table 1. Simulation parameters.

Parameters	Values	Parameters	Values
V_m	311 V	n	1:1
f_g	50 Hz	L_{leak}	45 uH
V_{dc}	220 V	L_g	180 uH
f_S	50 kHz	C_1	5 uF

In Figure 5, under two groups of LC filter parameters, the THDs of grid currents are all greater than 5% and the grid currents contain considerable 3rd and 5th harmonics. It follows that the grid voltage low-order harmonics will cause the same order grid current harmonics. Figure 5 can also illustrate that only varying the parameters of the filter is not a highly efficient approach to eliminate the grid current harmonics caused by the grid harmonics. Therefore, for the purpose of eliminating the influence of grid harmonics on grid currents, it is necessary to research a new closed-loop control strategy of grid currents.

4. Proposed Grid Current Closed-Loop Control

For the purpose of improving the grid current's performance and rejecting the effect of grid low-order harmonics, a general solution is to construct the closed-loop control system. The homologous closed-loop control configuration of grid currents of this converter is discussed first. Then the design of controller parameters is analyzed in detail in this section.

4.1. Grid Current Closed-Loop Control Configuration

To realize the control of the grid current fundamental component without steady error, the PR controller is utilized [21]. Because the single-phase grid voltage generally contains odd harmonics, the odd harmonics will be caused in the grid current. The odd-mode repetitive controller (OMRC) contains the internal modes of all odd harmonics resonant controllers, so it can effectively eliminate the grid current odd harmonics [22]. Besides, the needed data storage space of the OMRC is half the standard repetitive controller (RC), and its control error convergence period of the OMRC is also half the standard one [23]. Then, a novel compound grid current closed-loop control strategy containing a PR controller and an OMRC is proposed.

Figure 6 shows the configuration of the grid current closed-loop control strategy that is put forward. Variables with asterisk (*) are reference instructions. In Figure 6, I_{gm}^* is the amplitude of the grid current reference, which multiplies by the sine value of grid phase angle to gain the momentary grid current reference i_g^*. This grid phase angle is estimated online by the EPLL in [24]. The difference between i_g^* and i_g, i_{Er} is set to be the input of the OMRC. The sum of i_{Er} and the OMRC output are set to be the input of the PR controller. Furthermore, the active damping method in [25] is used to eliminate the resonance of LC filter. The inductor voltage is reconstructed by the differentiation of the acquired grid current to avoid adding an extra voltage sensor.
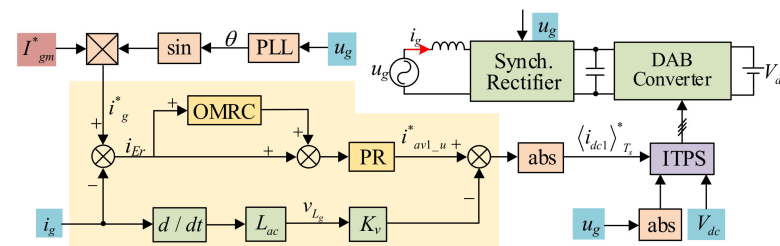
Figure 6. Schematic of the grid current closed-loop control strategy put forward.

After the output of the PR controller deducts the feedback inductor voltage, the absolute value is set to be the AC side current reference of ITPS. Furthermore, the instantaneous grid voltage and the DC side voltage input ITPS, then the control signals of switching cycles are finally obtained. According to Figure 6, the block diagram of the closed-loop system in

the discrete domain is gained, just as shown in Figure 7. The corresponding configuration of the OMRC is shown in Figure 8, in which $N_{Sa} = T_1/T_{Sa}$ is the number of the data that should be stored in a grid period. T_1 is the grid period and T_{Sa} is the sampling period. For the purpose of increasing this system stability, a LPF $Q(z)$ and a compensator $S(z)$ are set.
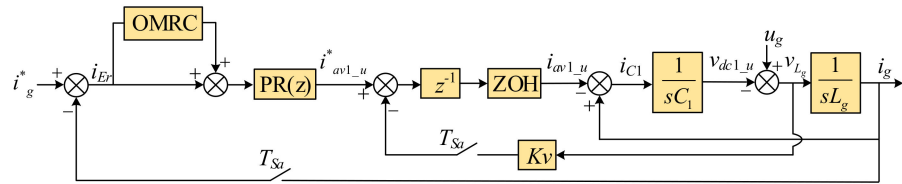

Figure 7. Block diagram of closed-loop control configuration in discrete domain.
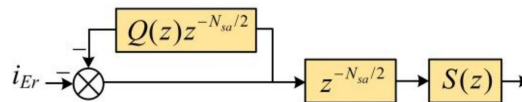

Figure 8. Block diagram of OMRC.

From Figure 8, the internal mode of OMRC is expressed as

$$G_{ORC}(z) = -\frac{z^{-N_{Sa}/2}}{1 + Qz^{-N_{Sa}/2}} \tag{17}$$

Equation (17) in s domain can be expressed as

$$
\begin{aligned}
G_{ORC}(s) &= \frac{1}{Q}\left[-1 + \frac{4}{N_{Sa}T_{Sa}}\sum_{k=1}^{\infty}\frac{s+\omega_{Qc}}{s^2+2\omega_{Qc}s+\omega_{Qc}^2+((2k-1)\omega_1)^2}\right] \\
&\approx \frac{1}{Q}\left[-1 + \frac{4}{N_{Sa}T_{Sa}}\sum_{k=1}^{\infty}\frac{s+\omega_{Qc}}{s^2+2\omega_{Qc}s+((2k-1)\omega_1)^2}\right]
\end{aligned}
\tag{18}
$$

where $\omega_{Qc} = -(\ln Q)/(N_{Sa}T_{Sa})$ is the resonant cutoff frequency.

From (18), the OMRC contains the internal modes of all odd harmonics resonant controllers, so it is able to effectively eliminate the odd harmonics. Figure 9 shows the curve of the OMRC's amplitude-frequency characteristics, which can be gained on the basis of (18). According to Figure 9, the OMRC presents the high gains in odd harmonic frequencies and accordingly, the effect of odd-order grid harmonics can be eliminated.
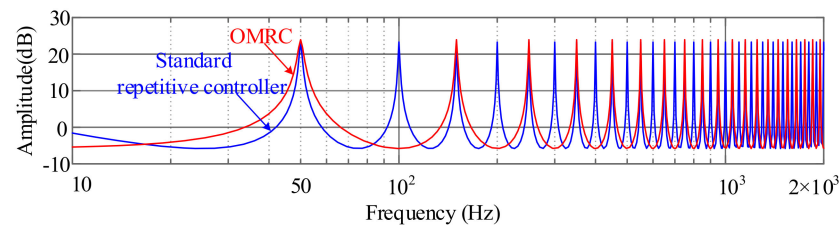
Figure 9. Bode diagram of OMRC.

4.2. Parameter Constraints of Proposed Compound Controller

Next, the parameter constraint of this proposed PR + OMRC control strategy is analyzed in this section, in order to build the theoretical reference for the controller parameter design.

The stability constraint is analyzed first. Figure 10 shows the simplified block diagram of the PR + OMRC, where the grid voltage is regarded as the disturbance. From Figure 10, the function expression of the grid current control error is

$$i_{Er}(z) = \frac{1 + Q(z)z^{-N_{Sa}/2}}{1 + z^{-N_{Sa}/2}[Q(z) - S(z)P'(z)]} \cdot \left[1 - P'(z)\right] \cdot \left[i_g^*(z) - G_{u_g 2 i_g}(z)u_g(z)\right] \tag{19}$$

where $P'(z) = PR(z) \cdot G_{i_{av}^* 2 i_g}(z) / \left[1 + PR(z) G_{i_{av}^* 2 i_g}(z) \right]$ is the system closed-loop transfer function only under PR controller. Then the block diagram of the grid current control error is obtained from (19) and shown in Figure 11, where $H(z) = Q(z) - S(z)P'(z)$.

Figure 10. Block diagram of proposed grid-current closed-loop control system.

Figure 11. Block diagram of PR+OMRC.

According to Figure 11, the grid current control error contains two parts, namely, it can be regarded as the sum of the two current control errors under only one controller, which are defined as e_{PR} and i_{Er}, respectively. In order to realize the global stability of the closed-loop system with the proposed compound controller, it is necessary to ensure e_{PR} and i_{Er} both converge. Therefore, the characteristic roots of the equivalent two closed-loop systems only under the PR controller and only under the OMRC should all be located within the unit circle of z plane:

$$|H(z)| = \left| Q(z) - S(z)P'(z) \right| < 1 \tag{20}$$

Next, the convergence constraints of the controller are analyzed. The major goal of this compound controller is to eliminate odd grid current's harmonics of caused by grid harmonics. From Figure 11, it yields

$$i_{Er}(z) = \frac{1 + Q(z)z^{-N_{Sa}/2}}{1 + z^{-N_{Sa}/2}H(z)} e_{PR}(z) \tag{21}$$

Furthermore, (21) can be organized as

$$i_{Er}(z) = -z^{-N_{Sa}/2} i_{Er}(z) H(z) + \left[1 + Q(z)z^{-N_{Sa}/2} \right] e_{PR}(z) \tag{22}$$

Angular frequency of grid current odd harmonics is

$$\omega_{odd} = 2\pi / (N_{Sa} T_{Sa}) \cdot (2k_{odd} + 1), \quad k_{odd} = 1, 2, 3 \ldots \tag{23}$$

From (23), at the odd harmonics frequencies, $z^{-N_{Sa}/2}$ is

$$z^{-N_{Sa}/2} = \left(e^{j\omega_o T_{Sa}} \right)^{-N_{Sa}/2} = e^{-j(2k_{odd}+1)\pi} = -1 \tag{24}$$

By substituting (24) into (22) and considering that Q is closed to 1 in the low frequency bands, there is

$$i_{Er}(z) = -z^{-N_{Sa}/2} i_{Er}(z) H(z) \tag{25}$$

According to (25), the update cycle of this proposed controller is $1/2T_1$. As a result, the control error convergence rate is twice that of the standard repetitive controller.

Last, the zero steady-state error constraint is derived. By substituting (24) into (21), there is

$$i_{Er}\left(e^{j\omega_o T_{Sa}} \right) = \left[1 - Q\left(e^{j\omega_o T_{Sa}} \right) \right] / \left[1 - H\left(e^{j\omega_o T_{Sa}} \right) \right] \cdot e_{PR}\left(e^{j\omega_o T_{Sa}} \right) \tag{26}$$

From (26), the control error of the current odd harmonics is reduced by $\left|1 - Q\left(e^{j\omega_o T_{Sa}}\right)\right| / \left|1 - H\left(e^{j\omega_o T_{Sa}}\right)\right|$ times. Therefore, in order to eliminate the odd harmonic currents, namely, to ensure $i_{Er}\left(e^{j\omega_o T_{Sa}}\right) \to 0$, it is necessary to set $Q(z) \to 1$, $H(z) \to 0$.

4.3. C. Parameter Design of Proposed Compound Controller

According to the above analysis, the parameters of PR and OMRC can be designed separately. The parameter design of the PR controller is first. From Figure 7, the discrete-domain open-loop transfer function of Q1S AC-DC converter is expressed as

$$G_{i_{av}^* 2 i_g}(z) = \frac{T_{Sa}}{L_g} \frac{c_1 z}{z^3 - c_2 z^2 + (c_1 K_v + 1)z - c_1 K_v} \tag{27}$$

In (27), $c_1 = \omega_n L_g \sin(T_{Sa}\omega_n)$, $c_2 = 2\cos(T_{Sa}\omega_n)$, $\omega_n = 1/\sqrt{L_g C_1}$.

In [21], the PR controller's parameter design has been discussed in detail and it is not mentioned here. Table 2 lists the resulted parameter values. The bode diagram of the closed-loop system with the PR controller $P'(z)$ drawn and shown in Figure 12. At grid frequency, characteristics of $P'(z)$ are unit gain and zero phase shift. Therefore, the control of grid current first harmonic without steady-state error can be achieved.

Table 2. PR Controller Parameters.

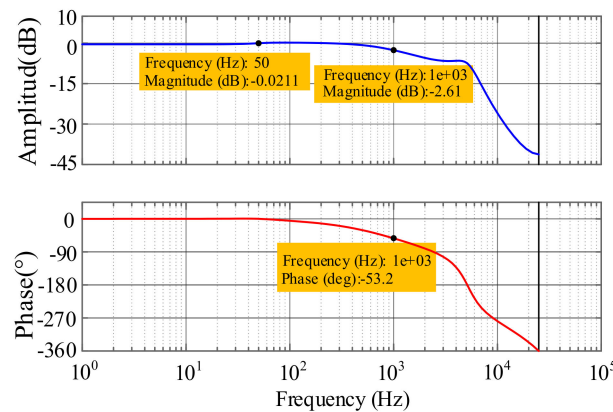| Parameter	ω_c	K_r	K_p	K_a	ω_a	ω_b
Value	2 rad/s	100	0.8	20	17,920 rad/s	280 rad/s

Figure 12. Bode diagram of system closed-loop transfer function with PR controller.

The parameters design procedure of OMRC is introduced as follows. The sampling frequency is the same as the switching frequency: $N_{Sa}/2 = f_S/f_g/2 = 500$. An LPF without phase shift is used for $Q(z)$ and its expression is

$$Q(z) = 0.25z^{-1} + 0.5 + 0.25z \tag{28}$$

The general expression of compensator $S(z)$ is

$$S(z) = K_{rc} z^c F(z) \tag{29}$$

where K_{rc} is the gain factor of the compensator, z^c is the phase lead link, and $F(z)$ is the low-pass filter.

From Figure 12, in the low-frequency bands, the gain of $P'(z)$ is unity, therefore, $K_r = 1$ and $F(z) = 1$ are determined. Since there is the phase lag in $P'(z)$, the phase lead link z^c should be used. From Figure 12, the lag phase of $P'(z)$ at 1 kHz is $\theta_l = 53.2°/180° \cdot \pi = 0.932$rad. Therefore, phase advance factor c is

$$c = \theta_l / (2\pi f_m T_{Sa}) \approx 7.4 \tag{30}$$

From (30), c contains the fractional part and it will decrease the actual phase compensation performance. In order to solve this problem, the finite-impulse response filter is utilized to approximate z^c [26]. The final expression of z^c in the discrete domain is

$$z^c = z^8 \left(0.28 + 0.84 z^{-1} - 0.12 z^{-2} \right) \tag{31}$$

Based on these determined parameters, the Nyquist curve of $H(z)$ is drawn and shown in Figure 13. From Figure 13, $|H(z)|$ is always less than 1 in the entire frequency range. In consequence, the designed closed-loop system is globally stable.
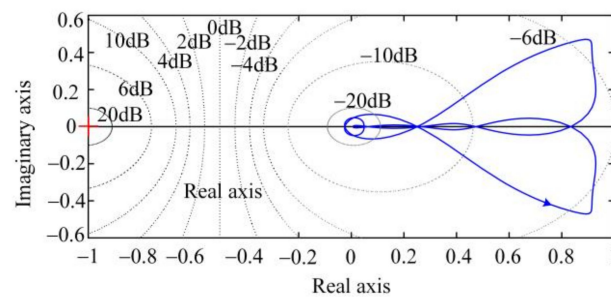
Figure 13. Nyquist curve of $H(z)$.

Figure 14 shows the bode diagram of the control error transfer function of the PR + OMRC. From Figure 14, the tracking error of grid current at fundamental frequency is far less than 0 dB. It means that the zero steady-state error grid current control can be achieved. Furthermore, tracking errors of grid current at the odd-order frequencies are also far less than 0 dB. It means that the influence of grid voltage odd harmonics on grid current can be efficiently eliminated by the proposed compound controller.
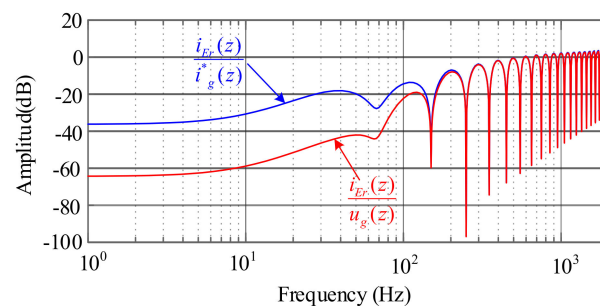

Figure 14. Curves of amplitude-frequency characteristics of control error transfer function of compound controller.

5. Experimental Verification

For the purpose of verifying the analysis of the effect of grid harmonics and proposed closed-loop control strategy, the experiment platform of this Q1S AC-DC converter has been built. Figure 15 clearly shows its photograph. The corresponding experimental parameters are the same as Tables 1 and 2. We inject 10% of the 3rd, 5% of the 5th and 7th harmonics to output voltage of AC source supply, with the aim to realize the simulation of the distorted single-phase grid voltage. All of these experimental results are measured by Memory Hicorder MR6000 from HIOKI (Ueda, Japan).
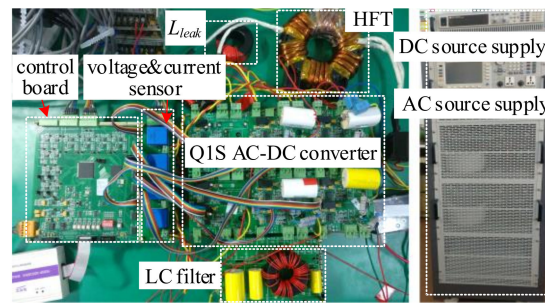
Figure 15. Photograph of experimental platform of Q1S AC-DC converter.

First, the influence of grid harmonics on grid current of this converter driven by ITPS control under open-loop situations is verified, as displayed in Figure 16. From Figure 16a,c, when given grid current amplitudes are 3A and 5A, respectively, obvious distortions of grid currents can be seen. From Figure 16b,d, under two different current amplitudes, 3rd, 5th, and 7th current harmonics obviously exist and THDs of grid currents are 8.22% and 5.27%, respectively. This verifies that the grid harmonics do cause the same order harmonics in the grid currents. In consequence, the validity of previous theoretical analysis is verified.
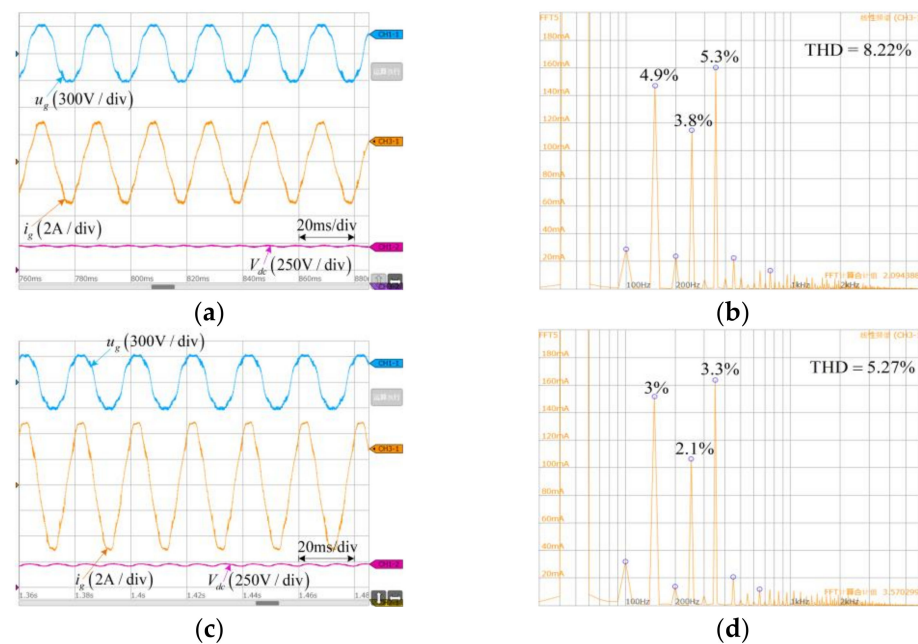
Figure 16. Experimental waveforms of Q1S AC-DC converter driven by ITPS. (**a**,**b**) Im is 3A, (**c**,**d**) Im is 5A.

In the following, the steady-state control performance of the compound closed-loop control strategy that we put forward is verified. Grid voltage and given grid current amplitude are the same as that under open-loop situations. Figure 17 shows relevant experiment results in detail. According to Figure 17a,c, under two given different grid current amplitudes, the actual grid currents are both sine waves, whose amplitudes are precisely 3A and 5A. It verifies that the closed-loop control strategy put forward realizes the function that control of grid current fundamental component is without steady-state error.
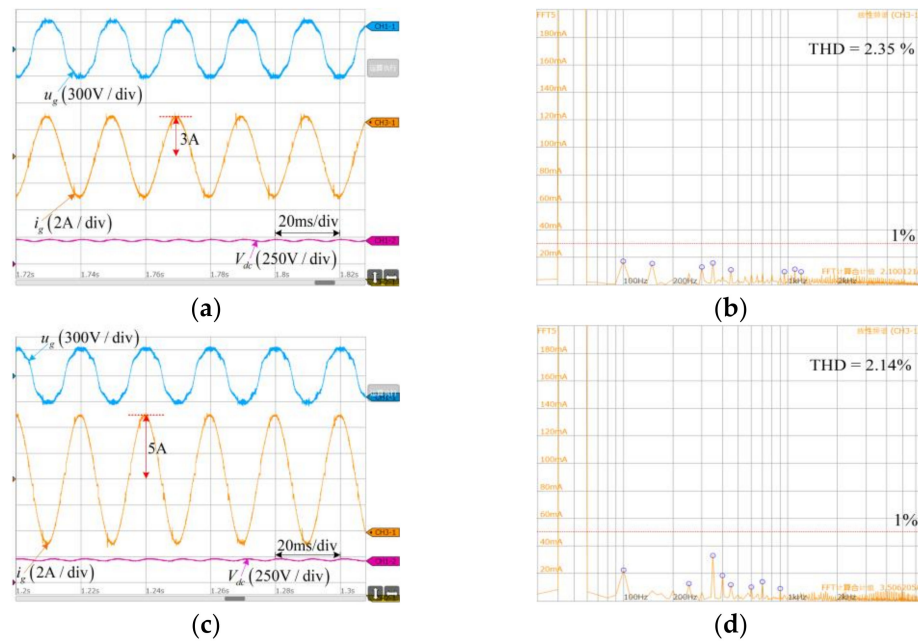
Figure 17. Experimental waveforms of proposed closed-loop controller. (**a**,**b**) Im is 3A, (**c**,**d**) Im is 5A.

From Figure 17b,d, THDs of grid currents are 2.35% and 2.14%, respectively, and the 3rd, 5th, and 7th harmonic contents are all reduced below 1% under these two situations. Therefore, the proposed closed-loop control strategy effectively eliminates the grid current odd harmonics.

For the purpose of verifying the control error convergence rate of OMRC that we put forward, Figure 18 shows the respective experiment results when proposed OMRC controller and another standard RC are suddenly enabled. From Figure 18, before the two controllers are enabled, there is a periodic ripple in i_{Er} and the grid current is distorted.
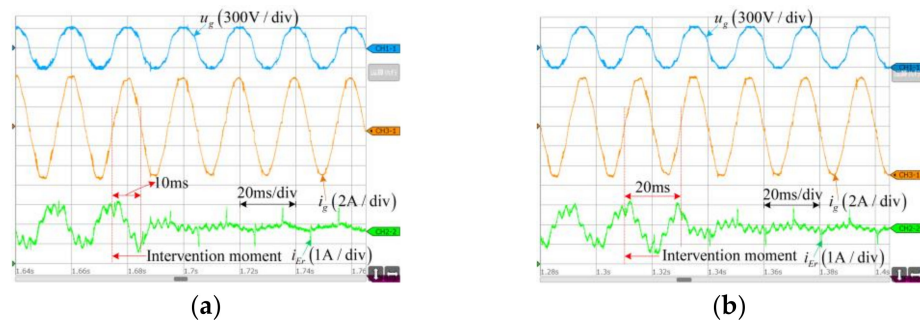

Figure 18. Experimental dynamic waveforms of two controllers. (**a**) OMRC, (**b**) standard RC.

After either OMRC or RC is enabled, i_{Er} reduces to zero gradually. The difference is that after OMRC is enabled, i_{Er} reduces to zero within 1/2 grid period; however, after the standard RC is enabled, i_{Er} reduces to zero within one grid period. Hence, it verifies the convergence speed of the OMRC is twice that of the standard RC.

Next, the dynamic performance of the proposed compound controller is verified in Figure 19. In Figure 19a, when the reference grid current steps up from 3A to 5A, the actual grid current amplitude can be adjusted to the given value within 2 ms. After around 60 ms (three grid periods), an undistorted sinusoidal grid current is obtained. Figure 19b shows the situation that the reference grid current steps down from 5A to 3A. Its dynamic process is similar to Figure 19a. Therefore, Figure 19 certifies that the proposed controller realizes good dynamic performance.
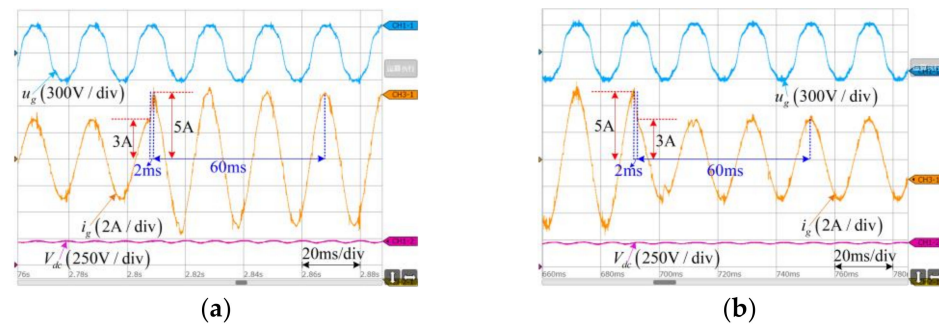
Figure 19. Experimental waveforms of proposed controller under grid current amplitude step. (**a**) From 3A to 5A, (**b**) from 5A to 3A.

Finally, the ability of the proposed strategy to reject the step disturbance of AC or DC sources is verified. From Figure 20, when the grid voltage amplitude floats up or down by 10%, the grid current amplitude maintains constant. Meanwhile, its transient adjustment process is very short. From Figure 21, when DC side voltage floats up or down by 20%, the grid current amplitude also maintains constant. Meanwhile, its transient adjustment process is also very short. Figures 1 and 20 verify that the compound controller we put forward efficiently eliminate the effect of step disturbance of grid voltage and DC side voltage.
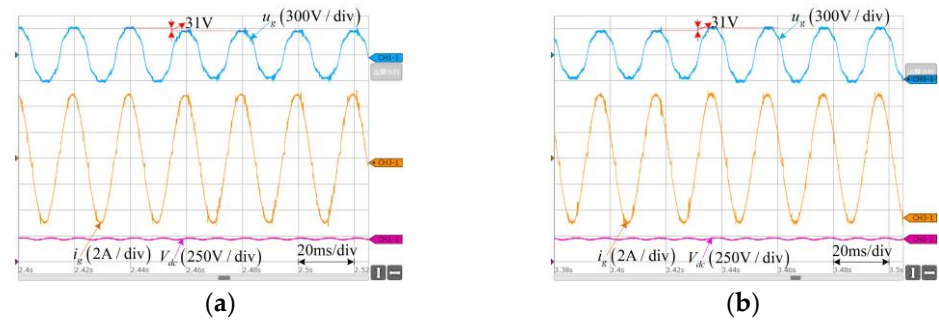

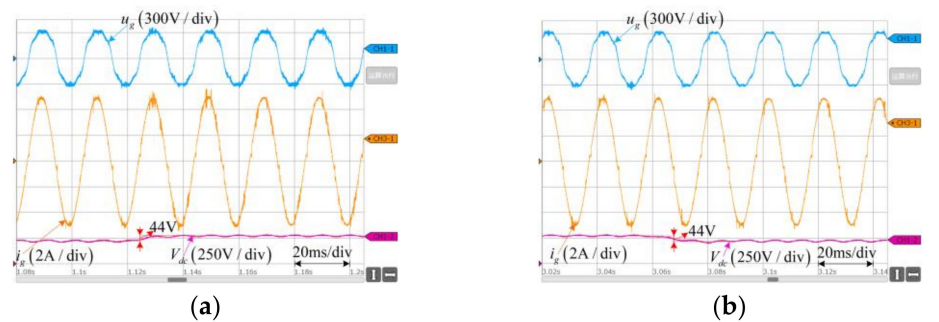**Figure 20.** Experimental waveforms of proposed controller under grid voltage amplitude jump. (**a**) Step up, (**b**) step down.

Figure 21. Experimental waveforms of proposed controller under DC side voltage variation, (**a**) step up, (**b**) step down.

6. Conclusions

A large-signal model of the Q1S AC-DC converter was built. Analysis results of the influence of the grid harmonics on grid current reveals the grid low-order harmonics do lead to grid current harmonics and deteriorate the performance of this kind of converter. The proposed PR + OMRC controller realizes good steady-state and dynamic performance of the grid current and effectively eliminates the influence of the grid harmonics in the entire power transfer range. The parameters of the designed controller can guarantee

the stability of the entire closed-loop system. Corresponding theoretical analysis and the proposed closed-loop control strategy construct the entire theoretical and technological system of the converter and thus is helpful for increasing feasibility and practicality of this single-stage isolated AC-DC converter.

Author Contributions: Conceptualization, F.W.; methodology, F.W.; software, J.S.; validation, F.W. and G.H.; formal analysis, F.W.; investigation, G.H.; writing—review and editing, F.W.; supervision, J.S. All authors have read and agreed to the published version of the manuscript.

Institutional Review Board Statement: Not applicable.

Informed Consent Statement: Not applicable.

Data Availability Statement: Data have been included in this paper.

Conflicts of Interest: The authors declare no conflict of interest.

References

1. Sfakianakis, G.E.; Everts, J.; Lomonova, E.A. Overview of the requirements and implementations of bidirectional isolated AC-DC converters for automotive battery charging applications. In Proceedings of the 10th International Conference on Ecological Vehicles and Renewable Energies, Monte Carlo, Monaco, 31 March–2 April 2015.
2. Koushki, B.; Safaee, A.; Jain, P.; Bakhshai, A. Review and comparison of bi-directional AC-DC converters with V2G capability for on-board EV and HEV. In Proceedings of the 2014 IEEE Transportation Electrification Conference and Expo (ITEC), Dearborn, MI, USA, 15–18 June 2014.
3. Zhang, Z.; Mallik, A.; Khaligh, A. A high step-down isolated three-phase AC-DC converter. *IEEE J. Emerg. Sel. Top. Power Electron.* **2018**, *6*, 129–139. [CrossRef]
4. Wu, F.; Fan, S.; Li, X.; Luo, S. Bidirectional buck-boost current-fed isolated DC-DC converter and its modulation. *IEEE Trans. Power Electron.* **2020**, *35*, 5506–5516. [CrossRef]
5. Wu, F.; Feng, F.; Gooi, H.B. Cooperative triple-phase-shift control for isolated DAB DC-DC converter to improve current characteristics. *IEEE Trans. Ind. Electron.* **2019**, *66*, 7022–7031. [CrossRef]
6. Luo, S.; Wu, F. Hybrid modulation strategy for IGBT-based isolated dual-active-bridge DC–DC converter. *IEEE J. Emerg. Sel. Top. Power Electron.* **2018**, *6*, 1336–1344. [CrossRef]
7. Friedli, T.; Kolar, J.W.; Rodriguez, J.; Wheeler, P.W. Comparative evaluation of three-phase AC-AC matrix converter and voltage DC-link back-to-back converter systems. *IEEE Trans. Ind. Electron.* **2012**, *59*, 4487–4510. [CrossRef]
8. Wang, H.; Blaabjerg, F. Reliability of capacitors for dc-link applications in power electronic converters—An overview. *IEEE Trans. Ind. Appl.* **2014**, *50*, 3569–3578. [CrossRef]
9. Rizzoli, G.; Zarri, L.; Mengoni, M.; Tani, A.; Attilio, L.; Serra, G.; Casadei, D. Comparison between an AC-DC matrix converter and an interleaved DC-dc converter with power factor corrector for plug-in electric vehicles. In Proceedings of the 2014 IEVC International Electric Vehicle Conference, Florence, Italy, 17–19 December 2014.
10. Everts, J.; Keybus, J.V.D.; Driesen, J. Switching control strategy to extend the ZVS operating range of a dual active bridge AC/DC converter. In Proceedings of the 2011 IEEE Energy Conversion Congress and Exposition (ECCE), Phoenix, AZ, USA, 17–22 September 2011.
11. Wu, F.; Li, X.; Luo, S. Improved modulation strategy for single-phase single-stage AC-DC converter considering power reversion zone. *IEEE Trans. Power Electron.* **2020**, *35*, 4157–4167. [CrossRef]
12. Li, X.; Wu, F.; Yang, G.; Liu, H.; Meng, T. Dual-period-decoupled space vector phase-shifted modulation for DAB based three-phase single-stage AC-DC converter. *IEEE Trans. Power Electron.* **2020**, *35*, 6447–6457. [CrossRef]
13. Fang, F.; Tian, H.; Li, Y. Coordination Control of Modulation Index and Phase Shift Angle for Current Stress Reduction in Isolated AC–DC Matrix Converter. *IEEE Trans. Power Electron.* **2021**, *36*, 4585–4596. [CrossRef]
14. Everts, J.; Krismer, F.; Keybus, J.V.D.; Driesen, J.; Kolar, J.W. Optimal ZVS modulation of single-phase single-stage bidirectional DAB AC-DC converters. *IEEE Trans. Power Electron.* **2013**, *29*, 3954–3970. [CrossRef]
15. Everts, J.; Keybus, J.V.D.; Krismer, F.; Driesen, J.; Kolar, J.W. Switching control strategy for full ZVS soft-switching operation of a Dual Active Bridge AC/DC converter. In Proceedings of the 27th Annual IEEE Applied Power Electronics Conference and Exposition (APEC), Orlando, FL, USA, 5–9 February 2012.

16. Everts, J. Closed-form solution for efficient ZVS modulation of DAB converters. *IEEE Trans. Power Electron.* **2017**, *32*, 7561–7576. [CrossRef]

17. Li, X.; Wu, F.; Yang, G.; Liu, H. Improved modulation strategy for single-phase isolated quasi-single-stage AC–DC converter to improve current characteristics. *IEEE Trans. Power Electron.* **2020**, *35*, 4296–4308. [CrossRef]

18. Cai, Y.; Xu, J.; Yang, P.; Liu, G. Design of double-line-frequency ripple controller for quasi-single-stage AC–DC converter with audio susceptibility model. *IEEE Trans. Ind. Electron.* **2019**, *66*, 9226–9237. [CrossRef]

19. Ma, H.; Li, Y.; Chen, Q.; Zhang, L.; Xu, J. A single-stage integrated Boost-LLC AC–DC converter with quasi-constant bus voltage for multichannel LED street-lighting applications. *IEEE Trans. Emerg. Sel. Top. Power Electron.* **2018**, *6*, 1143–1153. [CrossRef]

20. Uddin, W.; Wagaye, T.A.; Kim, M. Quasi-single-stage current-fed resonant AC–DC converter having improved heat distribution. *IEEE Trans. Power Electron.* **2022**, *37*, 13499–13512. [CrossRef]

21. Guo, Q.; Liu, H.; Zhang, Y. A new control strategy for a three-phase PWM current-source rectifier in the stationary frame. *J. Power Electron.* **2015**, *15*, 994–1005. [CrossRef]

22. Costa-Castello, R.; Grino, R.; Fossas, E. Odd-harmonic digital repetitive control of a single-phase current active filter. *IEEE Trans. Power Electron.* **2007**, *19*, 1060–1068. [CrossRef]

23. Zhou, K.; Low, K.; Wang, D.; Luo, F.; Zhang, B.; Wang, Y. Zero-phase odd-harmonic repetitive controller for a single-phase PWM inverter. *IEEE Trans. Ind. Electron.* **2006**, *21*, 193–201. [CrossRef]

24. Wu, F.; Sun, D.; Zhang, L.; Duan, J. Influence of Plugging DC Offset Estimation Integrator in Single-Phase EPLL and Alternative Scheme to Eliminate Effect of Input DC Offset and Harmonics. *IEEE Trans. Ind. Electron.* **2015**, *62*, 4823–4831. [CrossRef]

25. Bai, Z.; Ma, H.; Xu, D.; Wu, B.; Fang, Y.; Yao, Y. Resonance damping and harmonic eliminateion for grid-connected current-source converter. *IEEE Trans. Power Electron.* **2014**, *61*, 3146–3154.

26. Cui, P.; Wang, Q.; Li, S. Combined FIR and fractional-order repetitive control for harmonic current eliminateion of magnetically suspended rotor system. *IEEE Trans. Ind. Electron.* **2017**, *64*, 4828–4835. [CrossRef]